A micromechanics based model for rate dependent compression loaded unidirectional composites

(article starts on next page)

A micromechanics based model for rate dependent compression loaded unidirectional composites

Vivekendra Singh [a,b,*], Ragnar Larsson [b], Robin Olsson [a,b], Erik Marklund [a]

[a] *Division of Materials and Production, RISE AB, SE-431 22 Mölndal, Sweden*
[b] *Division of Material and Computational Mechanics, Department of Industrial and Materials Science Chalmers University of Technology, SE-412 96 Göteborg, Sweden*

ARTICLE INFO

ABSTRACT

Strain-rate effects in a unidirectional non-crimp fabric carbon/epoxy composite are addressed. To allow for kink-band formation including strain-rate effects and damage in such composites, the paper advances a recent model focused on compression loading at small off-axis angles. The model is based on computational *homogenization* with a subscale represented by matrix and fibre constituents at finite deformation. The fibre constituent is assumed to be elastic transversely isotropic and the matrix is viscoelastic–viscoplastic with damage degradation. Novel model improvements of special importance to small off-axis loading relate to the *isostress* formulation of the homogenized response in transverse shear. In this context, an enhanced homogenized elastic response is proposed based on Halpin–Tsai corrections to account for the nonuniform stress distribution on the microscale. The model captures the strongly rate sensitive kink-band formation due to localized matrix shearing and fibre rotation, confirming the experimentally observed increase in compressive strength for high strain rates.

1. Introduction

Carbon fibre reinforced composite materials are widely used in various fields of engineering due to their exceptional mechanical properties. Composites using non-crimp fabrics (NCF) are becoming increasingly attractive for lightweight structures. NCF are textile reinforcements made of one or several layers of parallel fibre bundles stacked on top of each other and held together with threads. The reinforcement is a unidirectional (UD) NCF, or "uni-weave", if the fabric only contains unidirectional fibre bundles woven together with thin weft threads. A UD NCF material is studied in this paper. Such materials have lower manufacturing costs, while still having acceptable specific stiffness and strength properties compared to UD prepreg. Therefore, they are well suited for developing low cost lightweight structures. Improved material models for the strain-rate-dependent deformation and damage behaviour of composites under dynamic loading are needed for many applications. The rate dependence of composites reinforced by unidirectional fibres has been investigated in several experimental studies [1–5], where split Hopkinson bars are frequently used for high strain rate testing. The rate sensitivity depends on material constituents and the type of applied load. For example, carbon fibres are rate independent while glass fibres show rate dependency. Most polymer matrix materials show a high level of rate dependency.

The results are reviewed by Sierakowski [6]. An extensive experimental study of the current uniweave material under quasi-static loading was done by Bru et al. [7], while limited compressive and tensile tests under dynamic conditions were done recently [8]. The nonlinear rate dependent response seen in the experiments can be described by a viscoelastic/viscoplastic model. Some phenomenological invariant based models exist, and they describe viscoelastic/viscoplastic effects in polymer composites but without damage growth [9–11]. A damage model is needed to model final failure dominated by shear. Continuum damage based formulations without rate effects are proposed by [12,13], including fibre kinking theory, e.g. [14–17]. Other authors [18–20] used a functional formulation of the generalized Maxwell model introduced by Simo and Hughes [21] to model the behaviour of composites at high strain rates. They also introduce a nonlinear viscoelastic behaviour by coupling the damage and the viscoelasticity but without viscoplasticity. In addition to that, the mechanical behaviour, in particular at failure, of UD NCF materials depend on the mechanical behaviour and spatial arrangement of their constituents. As a consequence, the damage and failure modelling of such material systems require a multiscale approach. A micromechanics based model for unidirectional polymer composites under quasi-static and high strain rates was proposed by Larsson et al. [22], where the matrix
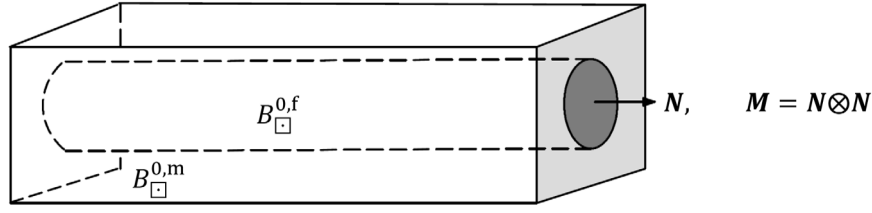
Fig. 1. Representative volume element of the material configuration of the composite microstructure. The fibre embedded in the matrix has the orientation tensor M.

is assumed to be viscoelastic–viscoplastic while the carbon fibres are elastic transversely isotropic. Recently, this model was extended to include continuum damage in unidirectional composites [23]. To allow for kink-band formation including strain-rate effects and damage in UD NCF composites, the present paper advances the model in [23] focused on dynamic compression loading at small off-axis angles. The model is based on computational *homogenization* with a subscale represented by matrix and fibre constituents at finite deformation. A simplifying isostress formulation is used for computational efficiency. Herein, novel improvements relate to the isostress formulation in the homogenization, where the shear stress transverse to fibres is improved. The paper is organized as follows. The constitutive models for fibres and matrix are described briefly in Section 2. These models are then incorporated in a constitutive model for a UD NCF material system via computational *homogenization*. Section 3 extends the framework from [23] to include the assumption of *isostress* transverse and across the fibres together with the modification to the macroscopic homogenized response. Numerical modelling, material parameters and their identification are conducted in Section 4. Section 5 presents experimental validation of the UD NCF for different strain rates in compression.

2. Formulation of the micro-mechanical/constitutive model

This section presents briefly the constitutive laws for the fibre and matrix constituents of the composite. Details of the constitutive models can be found in [23]. The representative volume element (RVE) is shown in Fig. 1. The RVE has the reference region $B_\square^0$ with volume $V_\square$. The fibre region is denoted $B_\square^{0,\mathrm{f}} \in B_\square^0$, and the region of the polymer is $B_\square^{0,\mathrm{m}} \in B_\square^0$. Perfect bond is assumed between the matrix and the fibres.

2.1. Elastic carbon fibres

A general large strain elastic model is applied with a view towards general three-dimensional simulations, see e.g. [22]. The fibres are elastic transversely isotropic characterized by a neo-Hookean strain energy $\psi^{\mathrm{f}} = \psi^{\mathrm{f}}(E)$, in turn containing four components in the Lagrange strain tensor E, [23]. As a result, the Kirchhoff stress is obtained as the push-forward transformation of the 2nd Piola Kirchhoff stress S^{f} for the fibre constituent as

$$\tau^{\mathrm{f}} = F \cdot S^{\mathrm{f}} \cdot F^t = \tau_d^{\mathrm{f}} + \tau_v^{\mathrm{f}} + \tau_s^{\mathrm{f}} + \tau_a^{\mathrm{f}} \quad \text{with } S^{\mathrm{f}} = \frac{\partial \psi^{\mathrm{f}}}{\partial E} \tag{1}$$

where τ_d^{f} and τ_v^{f} are due to the deviatoric (or volume preserving, isochoric) and the volume change energies, respectively. The longitudinal fibre shear and the axial fibre actions are contained in the stresses τ_s^{f} and τ_a^{f}. Moreover, F is the deformation gradient.

2.2. Viscoelastic/viscoplastic polymer matrix coupled to damage

The matrix constituent (or the resin) is assumed viscoelastic-viscoplastic combined with damage degradation $f[\alpha] = (1-\alpha)^2 + r$ in terms of the damage variable α. Following [23] the resulting Kirchhoff stress τ^{m} is obtained as the degrading effective stress deviator (where

a "hat" is used to denote effective stress, without damage) plus the volumetric contribution. This is written as

$$\tau^{\mathrm{m}} = f[\alpha]\hat{\tau}_d^{\mathrm{m}} + \tau_v^{\mathrm{m}}\mathbf{1} \quad \text{with } \hat{\tau}_d^{\mathrm{m}} = \hat{\tau}_{1,d}^{\mathrm{m}} + \hat{\tau}_{2,d}^{\mathrm{m}} \tag{2}$$

The stresses $\hat{\tau}_{1,d}^{\mathrm{m}}$ and $\hat{\tau}_{2,d}^{\mathrm{m}}$ are due to the deviatoric (or volume preserving, isochoric) energy and the stress $\hat{\tau}_v^{\mathrm{m}}$ is due to volume change of the matrix.

Fig. 2 shows the adopted rheology for the effective stress deviator of the polymer matrix subjected to volume preserving deformation. The involved viscous-elasticplastic model is represented by a spring with the shear modulus G_1 in parallel with a Maxwell element combined with a viscoplastic deformation mechanism in series. The viscoelastic part has quasi-static and dynamic shear moduli G_1, G_0 (via G_2) and the visco-elastic damper has the relaxation time t_{2*}. G_0 is the instantaneous stiffness parameter measuring via the rheology the dynamic elastic stiffness of the material as a function of the loading rate.

As to viscoplasticity, a Perzyna-type Bingham model with relaxation time t_* is adopted. Here, the viscoplastic yield is described by the Drucker–Prager function ϕ to capture pressure sensitivity in the polymer written as

$$\phi = \hat{\tau}_e^{\mathrm{m}} - (c_y + \gamma p) \quad \text{with } \hat{\tau}_e^{\mathrm{m}} = \sqrt{3/2}|\hat{\tau}_d^{\mathrm{m}}| \text{ and } p = -\tau_v^{\mathrm{m}} \tag{3}$$

where c_y is the cohesive yield stress parameter and γ is the friction parameter. These parameters are defined by the stresses σ_t and σ_c defining the quasi-static yield stress of the polymer in uniaxial tension and compression as

$$c_y = \frac{2}{1 + \frac{\sigma_t}{\sigma_c}}\sigma_t \ , \quad \gamma = 3\frac{\sigma_c - \sigma_t}{\sigma_c + \sigma_t} \tag{4}$$

As to the damage degradation $f[\alpha]$ in (2), the evolution of the damage variable α follows the Bingham damage law written as

$$l_c\dot{\alpha} = v^*\langle\alpha^{\mathrm{stat}}[\alpha] - \alpha\rangle \quad \text{with } \alpha^{\mathrm{stat}} = \frac{\mathcal{A}_{\mathrm{T}}[\alpha]l_c}{\mathcal{G}_{\mathrm{c}}} \tag{5}$$

where $\langle\bullet\rangle$ is the positive part function. Moreover, α^{stat} represents static damage in terms of the damage driving energy and $\mathcal{A}_{\mathrm{T}}$ and is the fracture energy $\mathcal{G}_{\mathrm{c}}$ for the neat resin, cf. [23] for details. The model generally yields mesh-objective response manifested by localized damage zones governed by the l_c- and v^*-parameters, cf. [15].

3. Homogenization at ply level

3.1. General approach

For computational efficiency, the homogenized response of a unidirectional composite ply is simplified by assuming *isostrain* response along the fibres, and *isostress* response for the transverse normal- and in-plane shear directions. For improved elastic model response, Halpin–Tsai based predictions for the numerical model have been made to account for non-uniform stress distribution in the matrix. This is explained in Section 3.2.

In this section the main steps towards the homogenized response of the fibre–matrix composite are outlined. Consider the RVE $B_\square^0$ of the material configuration for the UD composite in Fig. 1. The matrix
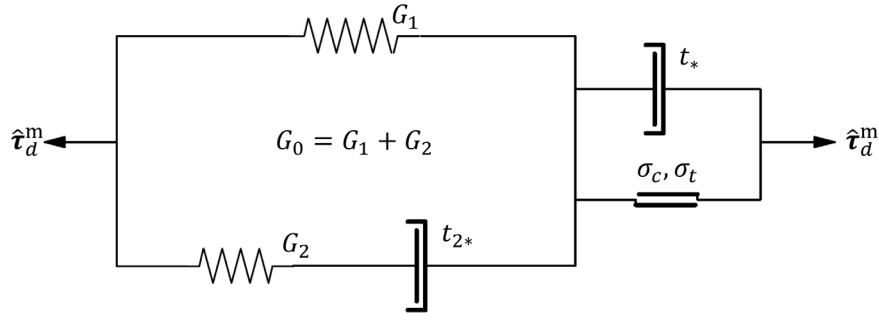
Fig. 2. Rheology for the viscoelastic–viscoplastic effective stress deviator of the polymer matrix.

material is in $B_\square^{0,m}$ and the fibre material is in $B_\square^{0,f}$. Consider next the RVE subjected to the constant Lagrange strain $\bar{E}$ in $B_\square^0$ defined as

$$\bar{E} = \frac{1}{2}\left(\bar{F}^t \cdot \bar{F} - \mathbf{1}\right) \tag{6}$$

where $\bar{F}$ is the macroscopic deformation gradient applied to the RVE in Fig. 1.

In order to represent the strain field E locally in $B_\square^0$, it is assumed that the strain consists of a constant (applied) part $\bar{E}$ and a sub-scale portion E^{sub} written as

$$E = \bar{E} + E^{\mathrm{sub}} \in B_\square^0 \Rightarrow \delta E = \delta \bar{E} + \delta E^{\mathrm{sub}} \in B_\square^0 \tag{7}$$

To further describe the subscale strain, the projected macroscopic strain is chosen to represent straining transverse to the fibre direction. To this end, the following assumptions for the isostrain/isostress state of the RVE are made:

1. The microstrain is constant in the fibre direction, so that the fibre and matrix constituents locally experience uniform strain, i.e. $E^{\mathrm{sub}} : M = 0$. A corresponding non-uniform stress state is then obtained across the fibre direction.
2. The microstress is assumed constant transverse to the fibre direction. To accommodate this, the micro fibre-shear E_s and the micro transverse fibre-straining $\hat{E}$ are assumed piecewise constant strain across the fibres.

Here, the transverse strain is defined by the projection $\hat{E} = \hat{\mathbb{I}} : \bar{E}$ and the longitudinal shear strain is $E_s = \mathbb{I}_s : \bar{E}$. Following the developments in [23], the fourth-order transverse and shear strain projection tensors $\hat{\mathbb{I}}$ and $\mathbb{I}_s$ are defined from

$$\hat{E} = \hat{\mathbf{1}} \cdot \bar{E} \cdot \hat{\mathbf{1}} \Rightarrow \hat{\mathbb{I}} = \hat{\mathbf{1}} \bar{\otimes} \hat{\mathbf{1}} \text{ with } \hat{\mathbf{1}} = \mathbf{1} - M \tag{8a}$$

$$E_s = \frac{1}{2}\left(\bar{E} \cdot M + M \cdot \bar{E}\right) - M : \bar{E}M \Rightarrow \mathbb{I}_s = \frac{1}{2}\left(M \bar{\otimes} \mathbf{1} + \mathbf{1} \bar{\otimes} M\right) - M \otimes M \tag{8b}$$

Upon introducing the *transverse strain* function $f = |\hat{E}|$ and the *fibre-shear strain* function $g = |E_s|$, the subscale strain is defined from the linear combination

$$E^{\mathrm{sub}} = af + bg \Rightarrow \delta E^{\mathrm{sub}} = \left(a\mathbb{F} : \hat{\mathbb{I}} + b\mathbb{G} : \mathbb{I}_s\right) : \delta \bar{E} + f\delta a + g\delta b \tag{9}$$

where the sub-gradients are

$$f = \frac{\partial f}{\partial \hat{E}} = \frac{\hat{E}}{|\hat{E}|}, \quad g = \frac{\partial g}{\partial E_s} = \frac{E_s}{|E_s|}$$

$$\mathbb{F} = \frac{\partial^2 f}{\partial \hat{E} \otimes \partial \hat{E}} = \frac{1}{|\hat{E}|}\left(\hat{\mathbb{I}} - f \otimes f\right), \quad \mathbb{G} = \frac{\partial^2 g}{\partial E_s \otimes \partial E_s} = \frac{1}{|E_s|}\left(\mathbb{I}_s - g \otimes g\right) \tag{10}$$

Note that a and b are scalar micro-fields in $B_\square^0$ representing the microscopic strain variation. Please note in view of (10) that the gradients $f = f[\bar{E}]$ and $g = g[\bar{E}]$. Likewise, we have that $\mathbb{F} = \mathbb{F}[\bar{E}]$ and $\mathbb{G} = \mathbb{G}[\bar{E}]$.

The Hill–Mandel condition then states the homogenized virtual work as the virtual work done by the micro-strain and stress fields in the RVE domain. In view of (7) and (9), this condition is formulated in Lagrange strain and the 2nd Piola Kirchhoff stress as

$$\delta \bar{E} : \bar{S} = \delta \bar{E} : \langle(\mathbb{I} + a\mathbb{F} + b\mathbb{G}) : S\rangle_{B_\square^0} + \langle \delta a S : f\rangle_{B_\square^0} + \langle \delta b S : g\rangle_{B_\square^0} \ \forall \delta a, \delta b \tag{11}$$

where $\mathbb{I}$ is the (standard) 4th order identity tensor and the volume mean of $B_\square^0$ is defined through $V_{B_\square^0} \langle \bullet \rangle_{B_\square^0} = \int_{B_\square^0} \bullet \, dB$, $V_{B_\square^0} = m\left[B_\square^0\right]$.

The Hill–Mandel relation in (11) yields the homogenized effective stress

$$\bar{S} = \langle(\mathbb{I} + a\mathbb{F} + b\mathbb{G}) : S\rangle_{B_\square^0} \tag{12}$$

corresponding to the micromechanical equilibrium relations

$$\langle \delta a S : f\rangle_{B_\square^0} + \langle \delta b S : g\rangle_{B_\square^0} = 0 \ \forall \delta a, \delta b \tag{13}$$

We also consider the corresponding kinematic compatibility condition

$$\delta \bar{S} : \bar{E} = \langle \delta S : E\rangle = \delta \bar{S} : \langle E\rangle \Rightarrow \delta \bar{S} : \langle af + bg\rangle = 0 \Rightarrow$$
$$\boxed{\langle a \rangle_{B_\square^0} = 0 \ , \ \langle b \rangle_{B_\square^0} = 0} \tag{14}$$

Hence, the local scalar fields a and b have vanishing mean value in the RVE domain. It is further assumed that parameters a and b are piecewise constant in $B_\square^0$ so that

$$a = \left\{a^{\mathrm{m}} \ \forall X \in B_\square^{0,m} , \ a^{\mathrm{f}} \ \forall X \in B_\square^{0,f}\right\},$$
$$b = \left\{b^{\mathrm{m}} \ \forall X \in B_\square^{0,m} , \ b^{\mathrm{f}} \ \forall X \in B_\square^{0,f}\right\} \tag{15}$$

corresponding to a piecewise constant stress field

$$S = \left\{S^{\mathrm{m}} \ \forall X \in B_\square^{0,m} , \ S^{\mathrm{f}} \ \forall X \in B_\square^{0,f}\right\} \tag{16}$$

The kinematic compatibility condition (14) yields the consequent piece-wise constant scalar fields as

$$\int_{B_\square^0} a \, dB = v^{\mathrm{m}}a^{\mathrm{m}} + v^{\mathrm{f}}a^{\mathrm{f}} = 0 \Rightarrow a^{\mathrm{f}} = -\frac{v^{\mathrm{m}}}{v^{\mathrm{f}}}a^{\mathrm{m}}$$
$$\int_{B_\square^0} b \, dB = v^{\mathrm{m}}b^{\mathrm{m}} + v^{\mathrm{f}}b^{\mathrm{f}} = 0 \Rightarrow b^{\mathrm{f}} = -\frac{v^{\mathrm{m}}}{v^{\mathrm{f}}}b^{\mathrm{m}} \tag{17}$$

where v^{m} is the volume fraction matrix material and v^{f} is the volume fraction fibres. They have the relation $v^{\mathrm{m}} + v^{\mathrm{f}} = 1$. With this assumption of piecewise constant stress fields, we obtain the following local projection problems

$$\delta a^{\mathrm{m}} v^{\mathrm{m}} f : \left(S^{\mathrm{m}} - S^{\mathrm{f}}\right) = 0 \ , \quad \delta b^{\mathrm{m}} v^{\mathrm{m}} g : \left(S^{\mathrm{m}} - S^{\mathrm{f}}\right) = 0 \tag{18}$$

exactly corresponding to the assumption of constant microstress transverse to the fibre direction. We also find that the homogenized stress in (12) is obtained explicitly as

$$\bar{S} = \langle(\mathbb{I} + a\mathbb{F} + b\mathbb{G}) : S\rangle_{B_\square^0} = v^{\mathrm{m}}S^{\mathrm{m}} + v^{\mathrm{f}}S^{\mathrm{f}} + v^{\mathrm{m}}\left(a^{\mathrm{m}}\mathbb{F} + b^{\mathrm{m}}\mathbb{G}\right) : \left(S^{\mathrm{m}} - S^{\mathrm{f}}\right) \tag{19}$$

where S^f and S^m are the 2nd Piola Kirchhoff stresses of the fibre and matrix constituents, respectively. It follows that the homogenized Kirchhoff stress transforms with $\bar{F}$ as $\bar{\tau} = \bar{F} \cdot \bar{S} \cdot \bar{F}^t$.

3.2. Isostress formulation and correction to include non-uniform stress state

The *homogenization* in the current model is based on the *isostress* assumption, where the matrix and fibres experience equal and uniform transverse normal stresses and shear stresses. The *isostress* assumption results in the following expressions for the transverse Young's modulus $E_2^\star$ and shear modulus $G_{12}^\star$:

$$1/E_2^\star = v^m/E^{m\star} + v^f/E_2^f \,, \qquad 1/G_{12}^\star = v^m/G^{m\star} + v^f/G_{12}^f \qquad (20)$$

The *isostress* assumption is known to cause a significant underestimation of $E_2^\star$ and $G_{12}^\star$ for composites with unidirectional cylindrical fibres, as observed experimentally and by micromechanical finite element analysis [24]. The reason is that the fibres cause a nonuniform stress state in the matrix [24,25], which violates the *isostress* assumption. There is also an effect of the fibre distribution in the plane transverse to the fibres [24]. Square and hexagonal fibre arrays result in relatively similar values of E_2 or G_{12}. A random fibre array results in a similar value of E_2, but somewhat higher value of G_{12} than for a square or hexagonal array.

Various analytical expressions have been derived to estimate E_2 and G_{12} of fibre composites. Micromechanical models for composites with continuous fibres were originally developed by Hashin and co-workers, by considering the constituents as concentric circular cylinders, but the models only provide upper and lower bounds for G_{12}. This problem was solved by Christensen and Lo [26] using a generalized self-consistent scheme, whereby a cylindrical sub-domain is surrounded by an equivalent fibre–matrix microstructure. This approach was later extended to orthotropic fibres by Marklund et al. [27]. The self-consistent concentric cylinder models are based on serial expressions and provide accurate estimates. Halpin–Tsai [28] derived more convenient, and relatively accurate, closed-form approximations for E_2 and G_{12}, which may be rewritten on the following form:

$$E_2 = \frac{E^m(1 + \xi_E \, \eta \, v^f)}{1 - \eta \, v^f}, \quad \text{where } \eta = \frac{E_2^f/E^m - 1}{E_2^f/E^m + \xi_E} \,, \quad \text{and } \xi_E = 2 \qquad (21)$$

$$G_{12} = \frac{G^m(1 + \xi_G \, \eta \, v^f)}{1 - \eta \, v^f}, \quad \text{where } \eta = \frac{G_{12}^f/G^m - 1}{G_{12}^f/G^m + \xi_G} \,, \quad \text{and } \xi_G = 1 \qquad (22)$$

The parameter ξ may be seen as an interpolation parameter, where $\xi = 0$ corresponds to the *isostress* assumption and $\xi = \infty$ to the *isostrain* assumption. Various corrections to ξ have been suggested, but the values in Eqs. (21) and (22) have been found suitable for most cases. Here we will use the Halpin–Tsai expressions to correct the effects of the isostress assumption in the viscoelastic model, by determining an "enhancement factor" C to the nominal stiffness of the matrix. Thus, effective values of $E^{m\star}$ and $G^{m\star}$ are determined from solving the following equations:

$$E_2^\star = E_2 \Rightarrow E^{m\star}/E^m = C_E \,, \quad G_{12}^\star = G_{12} \Rightarrow G^{m\star}/G^m = C_G \qquad (23)$$

The solution depends on the fibre volume fraction and results in different values of C_E and C_G. In general the correction factors are rate dependent, as E^m and G^m are rate dependent. For the current material and quasi-static conditions we obtain $C_E = 1.5$ and $C_G = 1.3$, but simulations were based on a common average value $C_E = C_G = C = 1.4$ as $E^{m\star}$ and $G^{m\star}$ should increase proportionally to E^m and G^m for an isotropic matrix. The increase in matrix stiffness for dynamic loading will result in a slightly lower value of C, but for simplicity the value for quasi-static conditions was used in all simulations. The improvement in the elastic stiffness prediction for the quasi-static case is easily seen in Fig. 3. The figure clearly shows that the corrected viscoelastic model follows the Halpin–Tsai expressions for E_2 and G_{12} and accounts for the nonuniform stress state caused by the fibres.
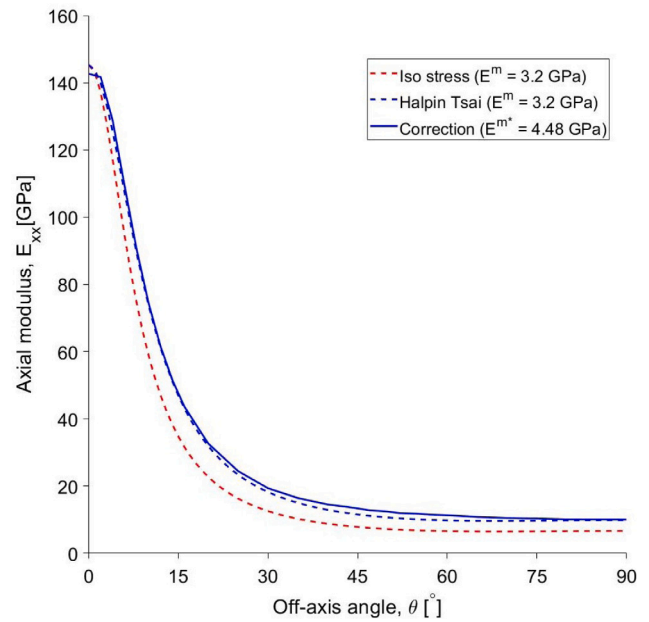

Fig. 3. Schematic representation of improvement in prediction of quasi-static elastic stiffness E^m of the matrix as function of the off-axis angle.

Table 1
List of fibre off-axis specimens, experimental axial strain rates in compression under quasi-static and dynamic loading [7,8].

Fibre angle θ	Strain rates ($\dot{\epsilon}$) in compression [/s]		
4°	1×10^{-4} (QS)	580	1130
90°	1×10^{-4} (QS)	496	984

Table 2
Material parameters for the carbon fibre.

E_L^f	E_T^f	G_{LT}^f	v_{LT}^f	v_{TT}^f	v^f
GPa	GPa	GPa	–	–	%
240	24	30	0.25	0.5	60

4. Material selection and parameters

The material consists of epoxy reinforced by a unidirectional non-crimp fabric (NCF). The NCF is a Porcher 4510 "uniweave" with 96.5 percent HTS45 carbon fibres and 3.5 percent glass/polyamide weft yarns. The epoxy consists of Araldite LY556 epoxy resin, an Aradur HY917 hardener and a DY070 accelerator [29]. The quasi-static experiment on the UD NCF composite was performed by Bru et al. [7] in tension and compression along and transverse to the fibres. Recently, Olsson et al. [8] performed dynamic tests on off-axis specimens of the same material system in tension and compression. The test specimen, subjected to uniaxial compression under dynamic loading is shown in Fig. 4 and it is also used to simulate the quasi-static tests by Bru et al. [7]. The specimen is free to move in the vertical direction and has a fully constrained mid-point on the left boundary as shown in Fig. 4. The applied loading rate is $v = \dot{\epsilon}L$, where $\dot{\epsilon}$ and L are the applied strain rate (Table 1) and specimen length (Fig. 4(a)). Table 1 lists the fibre off-axis specimens used for model validation together with the corresponding experimental axial strain rates and loading rates under quasi-static and dynamic loading. Note that the experiments were performed on specimens with a nominal fibre direction of 0° and 90°. The 4° fibre direction is used to represent the inherent fibre misalignment of the NCF material [30], as modelled in [17].

The carbon fibres are assumed to be linear elastic and transversely isotropic as presented in Section 2.1. Their material properties are
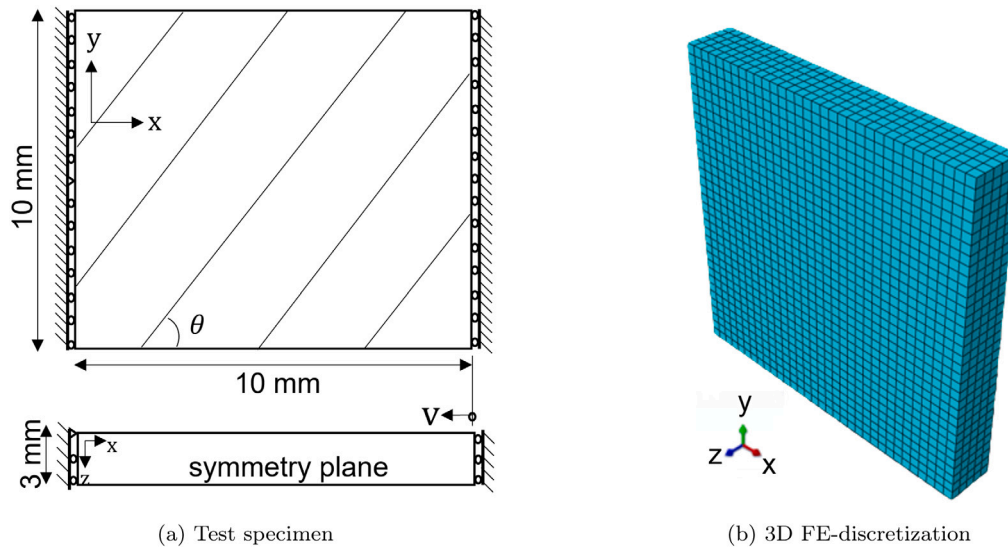
(a) Test specimen

(b) 3D FE-discretization

Fig. 4. Specimen geometry for HTS45-LY556 composite laminates subjected to compression loading through the prescribed horizontal velocity v at the right edge.

Table 3
Material parameters for the epoxy at quasi-static loading.

G_1	v^m	σ_t	σ_c	$\mathcal{G}_c$
GPa	–	MPa	MPa	N/mm
1.18	0.35	70	87	0.09

Table 4
Estimated model parameters for neat epoxy matrix material.

G_2	t_{2*}	t_*	l_c	v^*
GPa	s	s	mm	mm/s
1.68	5×10^{-5}	5×10^{-5}	0.05	$\dot{e} \times 10 \times 5$

reported in Table 2. The longitudinal modulus is according to the manufacturers data [31] and other fibre properties are estimated. For example, the transverse modulus of HTS45 fibres is not available in the literature. It is assumed to be about 1/10th of its longitudinal modulus, which is the typical case for most fibres. Similarly, the LY556 epoxy resin is assumed to follow a viscoelastic–viscoplastic-damage model as discussed in Section 2.2. The adopted material properties for LY556 epoxy (shown in Table 3) are obtained from [29], except [32] for compressive strength. The estimated value of $\mathcal{G}_c^\star$ for the LY556 epoxy resin is 0.27 N/mm. This is due to the fact that the current model assumes that damage generation is associated with distortional (shear) deformation of the resin. Plastic deformation of the resin in fibre reinforced composites is typically constrained by the fibres, which implies that the behaviour of most common resins is brittle or semi-brittle. In this case, "global" shear failure (Mode II) occurs by coalescence of inclined tensile (Mode I) microcracks between the fibres, resulting in the commonly observed "shear cusps". The effective Mode II toughness for coalescing tilted Mode I microcracks was derived by Xia and Hutchinson [33] and is given by $\mathcal{G}_{\mathrm{IIc}} = 3.1\,\mathcal{G}_{\mathrm{Ic}}$, where $\mathcal{G}_{\mathrm{Ic}}$ is the Mode I toughness. This prediction is also supported by extensive experimental data. Thus, since damage is caused by shearing, the simulations will be based on the effective toughness $\mathcal{G}_c^\star = 3.1\,\mathcal{G}_c$, where $\mathcal{G}_c$ is the (Mode I) toughness of the neat resin, reported as 0.09 N/mm [29].

An enhancement factor $C = 1.4$ is used to improve the elastic stiffness prediction under in-plane shear ($G_1^\star = 1.4\,G_1$) and transverse loading, based on the discussion in Section 3.2.

4.1. Estimated model parameters

This section summarizes the steps for the determination of model parameters associated with the material system, HTS45/LY556. The model parameters are shown in Table 4. The procedure for determining the model parameters has been thoroughly explained in [22,23]; a brief summary is given here.

The LY556 epoxy matrix follows a viscoelastic–viscoplastic-damage model as discussed in Section 2.2. Three model parameters are needed

for the viscoelastic–viscoplastic response. These parameters are: dynamic shear modulus G_2, viscoelastic damper t_{2*} and a viscoplastic damper t_*. In addition, the internal length l_c and the fracture area propagation velocity v^* are needed to model the damage evolution.

For uniaxial compression testing at the material point level, a FORTRAN VUMAT is implemented in MATLAB. The viscoelastic parameters G_2 and t_{2*} of the neat LY556 resin were calibrated by comparing our model response to the experimental data by Naik et al. [34]. The dynamic stiffness of the resin was determined by matching the secant shear modulus for 1% strain to their data at high strain rates. The viscoplastic damper t_* is assumed to have the same value as the viscoelastic damper t_{2*}. From the experimental data for UD NCF in [7,8], the estimation of model parameter l_c is based on finding the best possible model response for 4° and 90° off-axis specimen simultaneously under quasi-static and dynamic loading in compression. The damage progression speed v^* should be very high; higher than the crack propagation speed. Therefore, v^* is defined as 5 times higher than the applied loading rate. It was observed that with this v^* value, a converged model response is obtained. The model and experimental responses in Fig. 5 are shown by solid and dashed lines, where black curves represent quasi-static response.

The overestimated compressive strength for the dynamic small off-axis cases in Fig. 5(a), where fibres dominate, the response can be explained by the model assumption of linear elastic fibres. Thus, for small fibre angles (in this case 4°) the only possible failure mode in the model is fibre kinking, where increasing viscous effects in the matrix cause an increasing kinking stress. In practice there is, however, a competing failure mode involving compressive failure of the fibres.

For small fibre angles, an increasing matrix stiffness eventually causes a transition to a compressive fibre failure. This effect was observed by e.g., Ewins et al. [35] for decreasing temperatures, Fig. 6. The effect is, however, entirely analogous for increasing rates, according to the time–temperature correspondence in viscous effects of polymers. The slight increase in fibre compressive strength at decreasing temperature was attributed to interaction with a stiffer matrix, which constrains the shear failure of the fibre. For large fibre angles, the
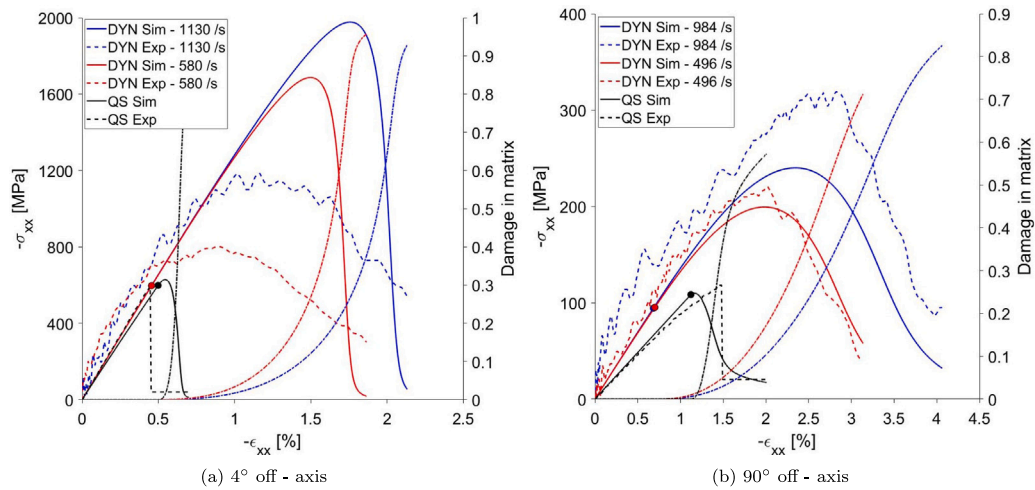
Fig. 5. Comparison of experiment and uniaxial stress–strain predictions in compression at the material point level. The comparison concerns quasi-static and dynamic loading at two different fibre orientations. Coloured circles represent onset of yielding. (For interpretation of the references to colour in this figure legend, the reader is referred to the web version of this article.)
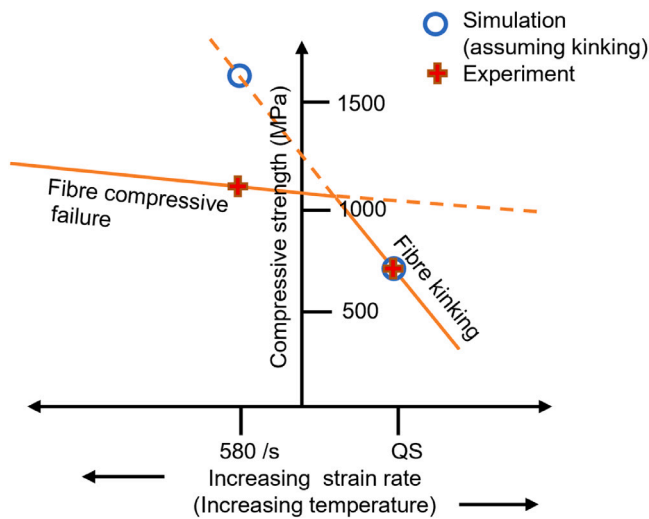

Fig. 6. Variation of compressive strength for small fibre angles with strain rate and temperature.
Source: Adapted from [35].

matrix dominates the response and therefore the assumption of linear elastic fibres does not affect the overall response.

5. Finite element validation

In the previous section, the set of model parameters were estimated from experimental measurements of the UD NCF composite at different strain rates in compression. These parameters are used to validate the material model by predicting the intralaminar failure of the UD NCF composite at different strain rates in compression.

The VUMAT considered in the previous section for uniaxial testing is implemented in Abaqus/Explicit for 3D FE-analyses of the ply-behaviour. The FE-model is discretized with 8-node reduced integration C3D8R solid elements. A mesh with dimensions of $0.3 \times 0.3 \times 0.3 \ mm^3$ as shown in Fig. 4 is used. For the stress–strain curves presented in this article, the normal strain to the loading *x*-direction is averaged over the xy-plane and plotted versus the resulting axial stress on the yz-face (Fig. 4).

Fig. 7(a) depicts the comparison between the FE-predictions and the experimental results for 4° off-axis UD NCF at quasi-static and dynamic loading in compression. The stiffness of FE based uniaxial stress–strain responses agree well for the quasi-static loading whereas underprediction is observed for dynamic loadings. Good agreement for strength prediction is observed for quasi-static loading, whereas overprediction of strength is obtained for both dynamic loading rates, 580/s and 1130/s. A diffuse out-of-plane failure is observed transverse to the loading direction in the yz-plane, Figs. 7(b)–7(c). The failure is observed in the vicinity of the loading surface of the analysed specimens. This occurs for both strain rates, Figs. 7(b)–7(c).

Fig. 8(a) shows the numerical predictions with the experimental results obtained at strain rates of 10^{-4}/s, 496/s and 984/s in compression for a 90° off-axis specimen. The measured and predicted initial stiffness and strength predictions are in good agreement for quasi-static and dynamic loading of 496/s, while they are underpredicted for 984/s. A localized in-plane uniaxial compressive strain field is observed for both strain rates, cf. Figs. 8(c)–8(d), transverse to the loading direction. Inclined out-of-plane deformations are also observed in the xz-plane, cf. Figs. 8(c)–8(d). A single out-of-plane failure is observed at 496/s, whereas multiple out-of-plane localized failure are observed at 984/s in the xz-plane. The intralaminar failure patterns agree well with the dynamic experimental test performed by Koerber et al. [1] on the IM7/8552 material system under transverse compression. Fig. 8(b) shows the FE-based stress–strain response in compression at 984/s for element lengths of 0.1 mm and 0.3 mm. The model responses are very similar. Hence, the rate-dependent damage model yields mesh independent response, as reported also in [15]. A localized in-plane deformation parallel to the fibres and an inclined out-of-plane deformation is obtained for the 0.1 mm mesh, similar to what is observed with the 0.3 mm mesh, cf. Figs. 8(d)–8(e).

5.1. Discussion

Fig. 9(a) shows a comparison of dynamic axial stress–strain response for 15°, 45° and 60° off-axis specimens in compression at 984/s. A brittle failure is observed for 15°, whereas ductile failure is obtained for 45° and 60°. The dynamic failure modes are shown in Figs. 9(b)–9(d). In-plane failure for the 15° is initiated by a localized compressive strain field formed transverse to the fibre direction as shown in xy-plane, cf. Fig. 9(b), whereas out-of-plane localized failure is visible in the vicinity of the loading surface as shown in yz-plane, cf. Fig. 9(b). This indicates a small influence of transverse-compression stresses acting on the fracture plane. This was also observed by Kawai et al. [36]. However, for large off-axis specimens i.e. 45° and 60°, a transverse compression dominated failure mode is observed. This explains an
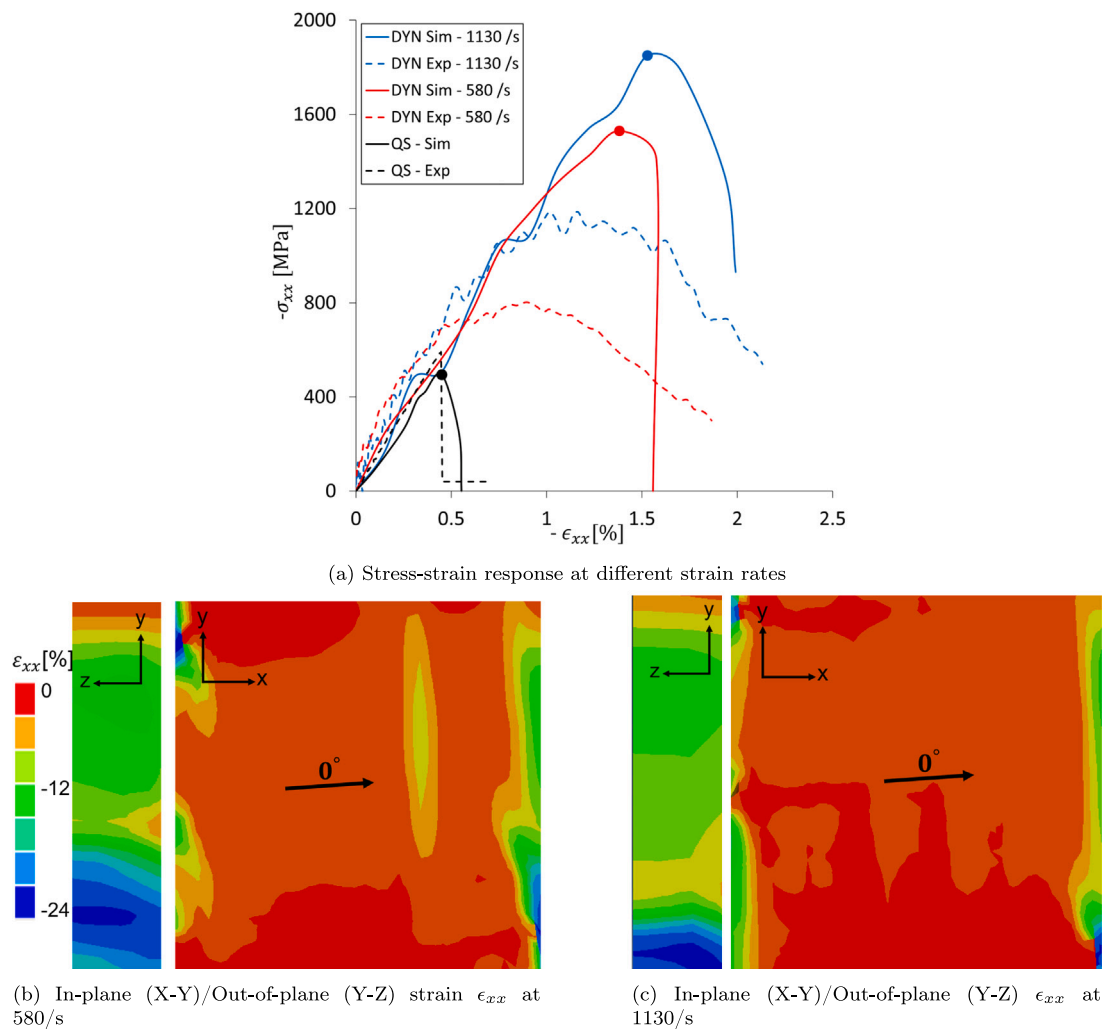
(a) Stress-strain response at different strain rates

(b) In-plane (X-Y)/Out-of-plane (Y-Z) strain ϵ_{xx} at 580/s

(c) In-plane (X-Y)/Out-of-plane (Y-Z) ϵ_{xx} at 1130/s

Fig. 7. FE predictions for dynamic failure of the 4° off-axis specimen in compression. The distribution maps of the axial strain ϵ_{xx} are indicated by the markers in 7(a).

inclined out-of-plane failure observed in the xz-plane, cf. Figs. 9(c)–9(d). In the xy-plane, cf. Fig. 9(c), an in-plane failure is observed along the fibre direction. This is in line with the experimental results of Koerber et al. [1]. However, in Fig. 9(d), in-plane failure is observed transverse to the loading direction.

An improved *homogenization* formulation is used in this paper. As described in Section 3, two local scalar fields, *a* and *b*, are used to fulfil the *isostress* assumption in the RVE transverse to the fibres and in the longitudinal fibre shear direction. Fig. 10 shows the influence of the *b*- parameter on the model response of 4° and 90° specimens. The predicted initial linear elastic response for the 4° specimen is in good agreement with the experiments but prediction of strength was not possible without the *b*-parameter, since the longitudinal shear is not properly captured. As can be seen in Fig. 10(a), when using both parameters a better agreement is obtained with the experiments. This is due to the contribution of the parameter *b*, resolving the isostress condition for the longitudinal fibre shear.

In the 90° case, however, out-of-plane failure dominates as seen in Fig. 8. As a result, improvement in the in-plane shear response does not contribute to the global out-of-plane failure, whereby similar dynamic responses were observed with one and two parameter *homogenization*, Fig. 10(b).

This discussion gives an interesting perspective on the transition of failure modes from small to large off-axis angles and the influence of parameter *b*. The activation of the *isostress*-coupling between the constituents in longitudinal fibre shear is of relevance only for "small" off-axis loaded specimens. For larger off-axis angles, it appears that the isostress nature of the longitudinal fibre shear is less significant due to out-of-plane dominated failure modes.

6. Conclusions and outlook

In this paper, a recently developed rate dependent material model [23] based on micromechanics and continuum damage is used to predict the intralaminar failure of a UD NCF material system under quasi-static and dynamic compressive loading. A viscoelastic–viscoplastic model is used for the matrix material and an elastic transversely isotropic model for the fibres. The matrix response is degraded by a continuum damage formulation based on a rate dependent damage evolution law [23]. An improved *homogenization* formulation is implemented at the ply level where the constituents are coupled via an *isostrain* assumption parallel to the fibres and *isostress* transverse to the fibres and in the longitudinal fibre shear direction. A major improvement in the *isostress* assumption is introduced by a novel splitting of the transverse strains and in-plane shear strains with parameters *a* and *b* representing variation in the microscopic strain. This allows prediction of shear failure and fibre kinking for small fibre angles, not captured by previous versions of the model. A modification is also implemented
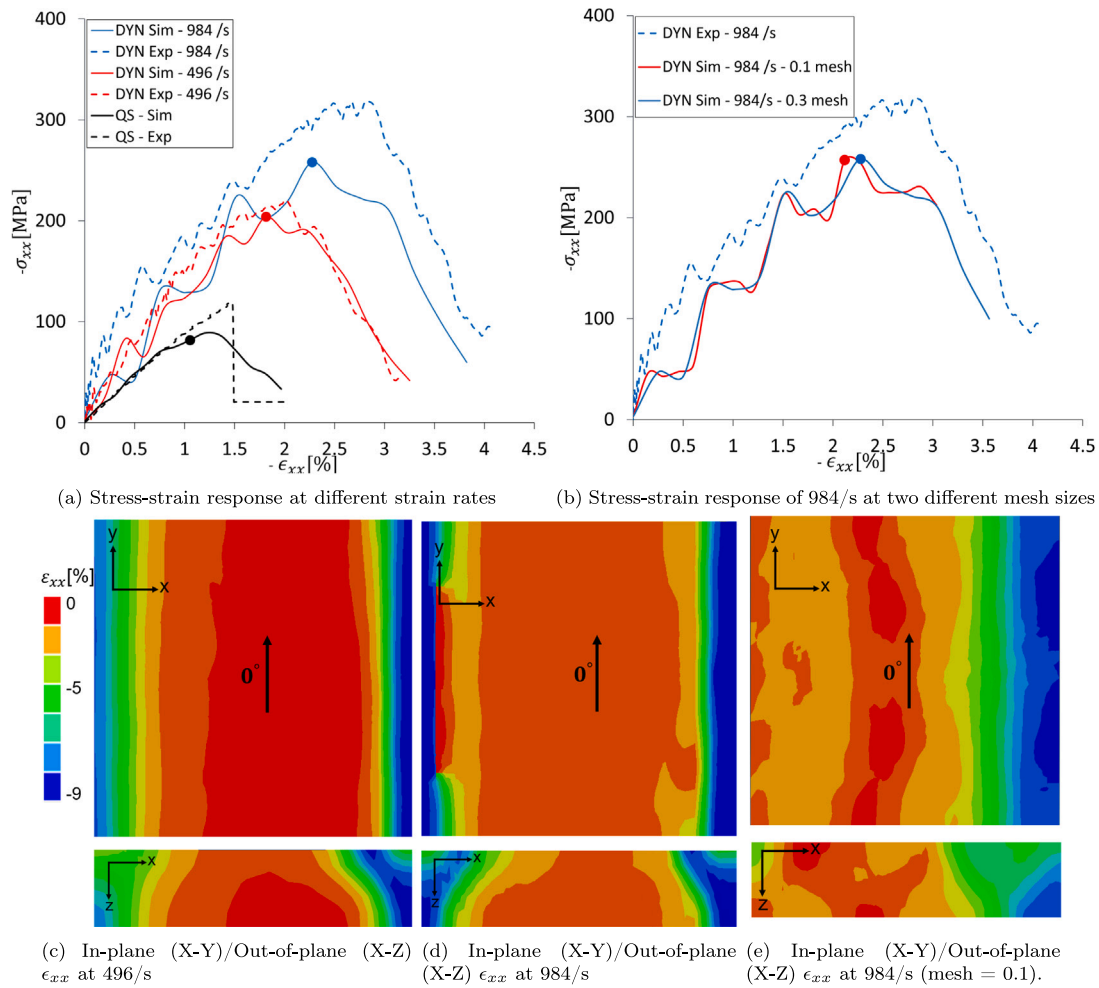
(a) Stress-strain response at different strain rates

(b) Stress-strain response of 984/s at two different mesh sizes

(c) In-plane (X-Y)/Out-of-plane (X-Z) ϵ_{xx} at 496/s

(d) In-plane (X-Y)/Out-of-plane (X-Z) ϵ_{xx} at 984/s

(e) In-plane (X-Y)/Out-of-plane (X-Z) ϵ_{xx} at 984/s (mesh = 0.1).

Fig. 8. FE predictions for dynamic failure of the 90° off-axis specimen in compression. The distribution maps of the axial strain ϵ_{xx} are indicated by the markers in 8(a).

in the model to consider non-uniform stress distribution in the matrix. Computational robustness of the model is demonstrated by simulating various off-axis specimen types under quasi static and dynamic loading and in compression. In general, the model parameters had to be estimated rather than calibrated, as the experimental data was limited to just two extreme fibre angles. Good correlation between predictions and experiments was achieved for the initial stress–strain response of the specimen with 4° fibre angle, which represents the typical fibre misalignment observed in the NCF material. The compressive strength for dynamic loading at 4° fibre angle was significantly overestimated but the increase in strength with strain rate observed in experiments is qualitatively confirmed by the model. For this loading, kink-band formation is the predicted failure mechanism associated with longitudinal shearing of the matrix, leading to significant increase in the strength at high strain rates. For small fibre angles, the strength is limited by the compressive strength of the individual fibres, which is not considered with the current assumption of elastic fibres. For 90° specimens, the predicted strength was just slightly lower than in the experiments. As expected, a brittle failure is observed for specimens with a small off-axis angle, whereas a ductile failure is observed in specimens with large off-axis angles. An increase in stiffness and strength predictions is observed under various strain rates in compression. Failure predictions from FE-analyses are in line with the results published for IM7/8552 material system [22,23] and experimental observations in [1,36].

CRediT authorship contribution statement

Vivekendra Singh: Methodology, Formal analysis, Software, Investigation, Data curation, Visualization, Validation, Writing – original draft. **Ragnar Larsson:** Conceptualization, Software, Investigation, Writing – review & editing. **Robin Olsson:** Formal analysis, Validation, Investigation, Writing – review & editing, Supervision. **Erik Marklund:** Validation, Investigation, Writing – review & editing.
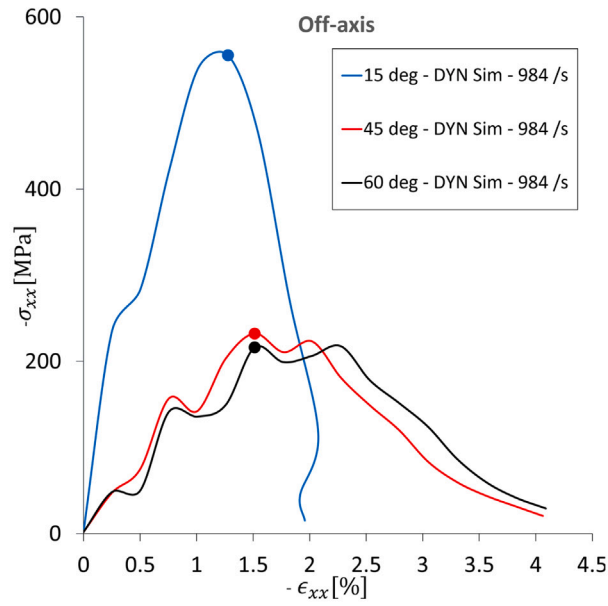
Declaration of competing interest

The authors declare that they have no known competing financial interests or personal relationships that could have appeared to influence the work reported in this paper.
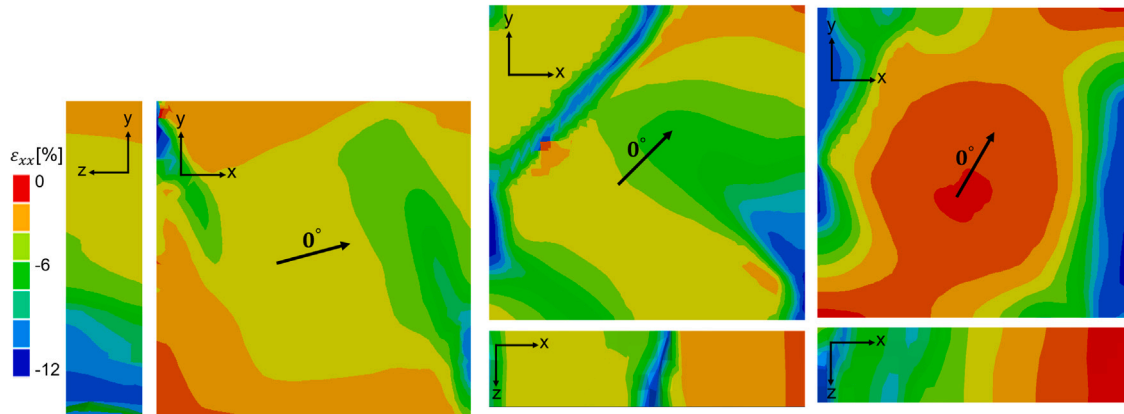
Data availability

Data will be made available on request.
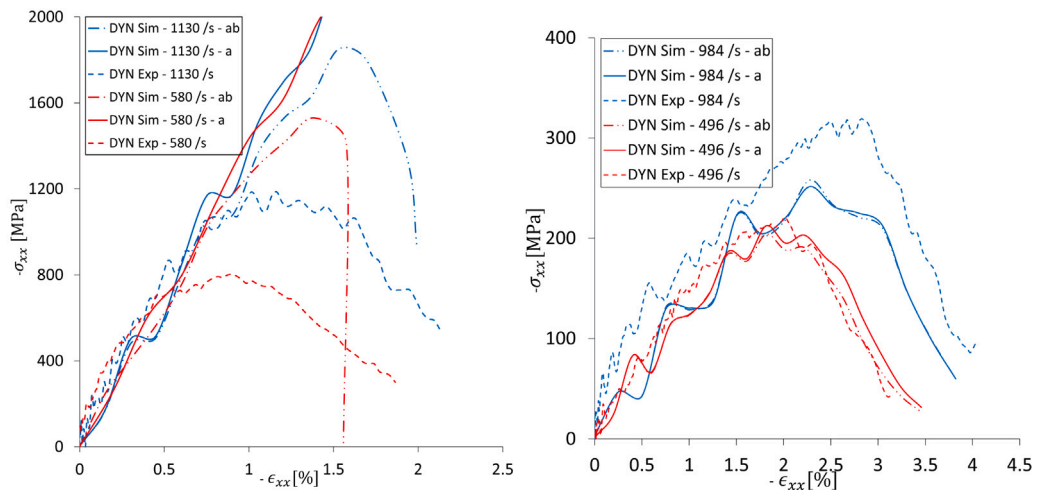
Acknowledgements

(a) Stress-strain response at different off-axis specimen

(b) In-plane (X-Y)/Out-of-plane (Y-Z) ϵ_{xx} in 15°

(c) In-plane (X-Y)/Out-of-plane (X-Z) ϵ_{xx} in 45°

(d) In-plane (X-Y)/Out-of-plane (X-Z) ϵ_{xx} in 60°

Fig. 9. FE predictions for dynamic failure of different off-axis specimens in compression at 496/s. The distribution maps of the axial strain ϵ_{xx} are indicated by the markers in 9(a).

(a) 4° response with parameter a and a & b

(b) 90° response with parameter a and a & b

Fig. 10. Comparison of model response for two off-axis specimens under dynamic loading in compression. Solid red curves considers solely the a-field whereas point-dotted red curves considers both a- and b-fields.

References

[1] H. Koerber, J. Xavier, P.P. Camanho, High strain rate characterisation of unidirectional carbon-epoxy IM7/8552 in transverse compression and in-plane shear using digital image correlation, Mech. Mater. 42 (11) (2010) 1004–1019.

[2] H.M. Hsiao, I.M. Daniel, R.D. Cordes, Strain rate effects on the transverse compressive and shear behaviour of unidirectional composites, J. Compos. Mater. 33 (17) (1999) 1620–1642.

[3] J. Harding, Effect of strain rate and specimen geometry on the compressive strength of woven glass-reinforced epoxy laminates, Composites 24 (4) (1993) 323–332.

[4] A. Gilat, R. Goldberg, G. Roberts, Experimental study of strain-rate-dependent behavior of carbon/epoxy composites, Compos. Sci. Technol. 62 (2002) 1469–1476.

[5] I. Daniel, B. Werner, J. Fenner, Strain-rate-dependent failure criteria for composites, Compos. Sci. Technol. 71 (2011) 357–364.

[6] R.L. Sierakowski, Strain rate effects in composites, Appl. Mech. Rev. 50 (12) (1997) 741–761.

[7] T. Bru, P. Hellström, R. Gutkin, D. Ramantani, G. Peterson, Characterisation of the mechanical and fracture properties of a uni-weave carbon fibre/epoxy non-crimp fabric composite, Data Brief 6 (2016) 680–695.

[8] R. Olsson, G. Lampeas, B. Ravindran, F. Izerhab, Dynamic testing of a unidirectional NCF composite - a comparison of test methods, in: Presentation at 10th International Conference on Composites Testing and Model Identification, Online 18–20 May, 2021.

[9] P.W. Gerbaud, F. Otero, P. Bussetta, P.P. Camanho, An invariant based transversely-isotropic constitutive model for unidirectional fibre reinforced composites considering the matrix viscous effects, Mech. Mater. 138 (2019).

[10] S. Eskandaria, F. Pires, P.P. Camanho, H. Cuic, N. Petrinica, A. Marques, Analyzing the failure and damage of FRP composite laminates under high strain rates considering visco-plasticity, Eng. Fail. Anal. 101 (2019) 257–273.

[11] H. Koerber, P. Kuhn, M. Ploeckl, F. Otero, P.W. Gerbaud, R. Rolfes, P.P. Camanho, Experimental characterization and constitutive modeling of the nonlinear stress–strain behavior of unidirectional carbon–epoxy under high strain rate loading, Adv. Model. Simul. 5 (2018) 17.

[12] P.P. Camanho, M. Bessa, G. Catalanotti, M. Vogler, R. Rolfes, Modeling the inelastic deformation and fracture of polymer composites – Part II: Smeared crack model, Mech. Mater. 59 (2013) 36–49.

[13] P. Maimí, P.P. Camanho, J.A. Mayugo, C.G. Davila, A continuum damage model for composite laminates: Part I – Constitutive model, Mech. Mater. 39 (2007) 897–908.

[14] S. Costa, R. Gutkin, R. Olsson, Mesh objective implementation of a fibre kinking model for damage growth with friction, Compos. Struct. 168 (2017) 384–391.

[15] R. Larsson, R. Gutkin, S.M. Rouhi, Damage growth and strain localization in compressive loaded fiber reinforced composites, Mech. Mater. 127 (2018) 77–90.

[16] D. Wilhelmsson, R. Talreja, R. Gutkin, L. Asp, Compressive strength assessment of fibre composites based on a defect severity model, Compos. Sci. Technol. 181 (2019) 107685.

[17] S. Costa, M. Fagerström, R. Olsson, Development and validation of a finite deformation kinking model for crushing of composites, Compos. Sci. Technol. 197 (2020) 108236.

[18] S. Treutenaere, F. Lauro, B. Bennani, G. Haugou, T. Matsumoto, E. Mottola, Constitutive modelling of the strain-rate dependency of fabric reinforced polymers, Int. J. Impact Eng. 108 (2017) 361–369.

[19] L. Dufour, B. Bourel, F. Lauro, G. Haugou, N. Leconte, A viscoelastic-viscoplastic model with non associative plasticity for the modelling of bonded joints at high strain rates, Int. J. Adhes. Adhes. 70 (2016) 304–314.

[20] M. Nciri, D. Notta-Cuvier, F. Lauro, F. Chaari, Y. Maalej, B. Zouari, Modelling and characterisation of dynamic behaviour of short-fibre-reinforced composites, Compos. Struct. 160 (2017) 516–528.

[21] J.C. Simo, T.J. Hughes, Computational Inelasticity, Springer New York, 1998, pp. 336–373.

[22] R. Larsson, V. Singh, R. Olsson, E. Marklund, A micromechanically based model for strain rate effects in unidirectional composites, Mech. Mater. 148 (103491) (2020) 193–212.

[23] R. Larsson, V. Singh, R. Olsson, E. Marklund, A micromechanically based model for dynamic damage evolution in unidirectional composites, Int. J. Solids Struct. 238 (111368) (2022).

[24] Y. Huang, K.K. Jin, S.K. Ha, Effects of fiber arrangement on mechanical behavior of unidirectional composites, J. Compos. Mater. 42 (18) (2008) 1851–1871.

[25] E. Totry, J.M. Molina-Aldareguia, C. González, J. LLorca, Effect of fiber, matrix and interface properties on the in-plane shear deformation of carbon-fiber reinforced composites, Compos. Sci. Technol. 70 (6) (2010) 970–980.

[26] R.M. Christensen, K.H. Lo, Solutions for effective shear properties in three phase sphere and cylinder models, J. Mech. Phys. Solids 27 (4) (1979) 315–330.

[27] E. Marklund, J. Varna, R.C. Neagu, E.K. Gamstedt, Stiffness of aligned wood fiber composites: effect of microstructure and phase properties, J. Compos. Mater. 42 (22) (2008) 2377–2405.

[28] J.C. Halpin, J.L. Kardos, The Halpin-Tsai equations: a review, Polym. Eng. Sci. 16 (5) (1976) 344–352.

[29] U.S. Huntsman Corporation, Araldite LY556 aradur 917 accelerator DY070 (data sheet 03/07/2007), 2007, URL: https://farix.hu/pdf/1360669728.pdf.

[30] D. Wilhelmsson, R. Gutkin, F. Edgren, L. Asp, An experimental study of fibre waviness and its effects on compressive properties of unidirectional NCF composites, Composites A 107 (2018) 665–674.

[31] J. Teijin Limited, HTS45 Tenax™ filament yarn product data sheet, 2021, URL: https://www.teijincarbon.com/products/tenaxr-carbon-fiber/tenaxr-filament-yarn?r=1.

[32] S. Singh, V.K. Srivastava, R. Prakash, Influences of carbon nanofillers on mechanical performance of epoxy resin polymer, Appl. Nanosci. 5 (2015) 305–313.

[33] C.S. Xia, J.W. Hutchinson, Mode II fracture toughness of a brittle adhesive layer, Int. J. Solids Struct. 31 (8) (1994) 1133–1148.

[34] N. Naik, R. Gadipatri, N. Thoram, V. Kavala, V. Ch., Shear properties of epoxy under high strain rate loading, Polym. Eng. Sci. 50 (2010) 780–788.

[35] P.D. Ewins, R.T. Potter, S.M. Bishop, P.J. Worthington, Some observations on the nature of fibre reinforced plastics and the implications for structural, Philos. Trans. R. Soc. 294 (1980) 507–517.

[36] M. Kawai, S. Saito, Off-axis strength differential effects in unidirectional carbon/epoxy laminates at different strain rates and predictions of associated failure envelopes, Composites A 40 (2009) 1632–1649.